RESEARCH ARTICLE

Temperature maps measurements on 3D surfaces with infrared thermography

**Gennaro Cardone · Andrea Ianiro ·
Gennaro dello Ioio · Andrea Passaro**

Abstract The use of the infrared camera as a temperature transducer in wind tunnel applications is convenient and widespread. Nevertheless, the infrared data are available in the form of 2D images while the observed surfaces are often not planar and the reconstruction of temperature maps over them is a critical task. In this work, after recalling the principles of IR thermography, a methodology to rebuild temperature maps on the surfaces of 3D object is proposed. In particular, an optical calibration is applied to the IR camera by means of a novel target plate with control points. The proposed procedure takes also into account the directional emissivity by estimating the viewing angle. All the needed steps are described and analyzed. The advantages given by the proposed method are shown with an experiment in a hypersonic wind tunnel.

List of symbols

C_1, C_2	*The first and the second universal radiation constants*, respectively equal to 3.7418×10^{-16} $\mathrm{Wm^2}$ and 1.4388×10^{-2} m K
$\underline{ds}$	Infinitesimal displacement vector in the image plane Π
$\underline{dS}$	Infinitesimal displacement vector in the world frame WF
$D_u \, D_v$	Pixel size in u and v direction
f	Focal length
I	Spectral radiance, or energy per unit time per unit surface area of emitting surface per unit solid angle per unit frequency or wavelength
k_1, k_2	Radial distortion coefficients
M	Mach number
$\underline{n}$	Normal unit vector on the object surface
o	Principal point of the camera frame CF
O	Centre of projection
P	Object point
p	Image point
$\underline{PM}$	Perspective transformation matrix
p_1, p_2	Tangential distortion coefficients
$\underline{R}$	Orthonormal rotation matrix
R, B, F	Camera calibration constants
$\underline{t}$	Translation vector between World Frame and Camera Frame
T	Temperature
u, v	Axes of the image frame IF
u_0, v_0	The coordinates of o in the image frame IF
U_D	Detected signal
$\underline{W}$	Viewing ray direction
x, y, z	Axes of the camera frame CF
X, Y, Z	Axes of the word frame WF
α	Absorptivity
ε	Emissivity
θ	Viewing angle
λ	Wavelength
ξ	Pixel aspect ratio
Π	Image plane
ρ	Reflectivity
τ	Transmissivity
ω, φ, κ	Euler angles

G. Cardone (✉) · A. Ianiro
Department of Aerospace Engineering (DIAS), University of Naples Federico II, Via Claudio 21, 80125 Naples, Italy
e-mail: gcardone@unina.it

G. dello Ioio
BP Institute for Multiphase Flow, University of Cambridge, Cambridge, England CB3 0EZ, UK

A. Passaro
Alta SpA, 56014 Ospedaletto, PI, Italy

Subscripts

amb	Related to the ambient surrounding the observed object
atm	Related to the atmosphere surrounding the observed object
i	Ideal
d	distorted
obj	Related to the object
X, Y, Z	Partial derivative

Superscripts

B	Emitted by a black body
R	Received from IR camera
T	Matrix transpose

1 Introduction

Infrared thermography is widely used as a non-contact temperature measurement technique in experimental fluid mechanics and heat transfer. The infrared cameras acquire an image that represents the thermal radiation emitted in the IR band from the observed surface; temperature is then obtained by means of a calibration law (DeWitt and Nutter 1989). When compared to other commonly used measurement techniques such as thermocouples or pyrometers, the use of an infrared camera as a temperature transducer appears advantageous from several points of view. In fact, since IR cameras are fully two dimensional (up to 1 M pixels), they produce a full temperature field; furthermore, IR measurements are non-intrusive (e.g., allowing conduction removal through thermocouple or RTD wires), and commercial cameras have sensitivity down to 20 mK and response time down to 20 μs. As such, IR thermography can be effectively employed to measure temperature and convective heat fluxes with both steady and transient sensors (Carlomagno and Cardone 2010) from natural convection to hypersonic flows (de Luca et al. 1992, 1995).

IR thermography is a purely two-dimensional technique and it is required to establish a correspondence between the points of the observed object and the pixels of the image. This is one of the main limitations of this technique if the observed object has a non-planar geometry, as it often happens in wind tunnel testing. Furthermore, in these cases, in order to get accurate temperature measurements, it is necessary to estimate the viewing angle on the observed surface to take into account the directional emissivity law (Siegel and Howell 1992). In aerodynamic wind tunnel testing, excluding the case of model oscillation connected to low stiffness of the sting, object shape and position are generally known with precision so, by using a camera model, after defining an object surface grid, it is possible to accurately rebuild on the object the radiance surface map measured by the IR camera.

Various algorithms for camera calibration have been reported over the years in the photogrammetry and computer vision literature. The algorithms are generally based on perspective or projective camera models, but applications of these models to the IR field are very rare. A specific classification for camera models and calibration methods can be made according to the parameter estimation and optimization technique employed:

- Linear techniques are quite simple and fast, but generally cannot handle lens distortion and need an array of control points of known coordinates. They can include closed-form solutions, but they usually simplify the camera model, neglecting the effects of the lens distortion. The well-known Direct Linear Transformation (DLT) into object space coordinates in close-range photogrammetry (Abdel-Aziz and Karara 1971) exemplifies such a technique.
- Nonlinear techniques such as the extended collinearity equation model, which forms the basis of the self-calibrating bundle adjustment, are most familiar to photogrammetrists. A rigorous and accurate modeling of the camera interior orientation and lens distortion parameters is provided (Brown 1971) through an iterative least-squares estimation process.
- A combination of linear and nonlinear techniques employ a linear method to recover initial approximations for the parameters, and the orientation and calibration are subsequently iteratively refined (Faugeras and Toscani 1986; Tsai 1987; Weng et al. 1992; Heikkilä and Silven 1997).

Büyüksalih (2003) first analyzed the geometric calibration of infrared imaging systems with a view to use them both in photogrammetry and in remote sensing (2D applications) and performed image correction for IR imaging systems with a polynomial law by using a single calibration plane.

An example of temperature distributions rebuilt on the 3D object surface from IR images has been proposed by Le Sant et al. (2002) and Le Sant (2005) who adopted a linear technique and found the model parameters using markers disposed on the observed object. The linear model needs only six markers to compute calibration constants but, since it neglects the effects of lens distortion, the linear model is characterized by errors whose entity depends on the complexity and the quality of the optical system. If more than six markers are available the camera calibration constants are computed with a root mean square method that minimizes the distance between the image marker coordinates and the coordinates computed with the camera model. Moreover, less than six markers are often present in

thermal images; in that case the calibration constant have to be found manually by fitting the model contour on the image.

In this work, after recalling the principle of IR thermography, the optical calibration method proposed by Heikkilä and Silven (1997) is applied to IR thermography by means of a novel target plate with control points (proposed by the present authors). A methodology to rebuild temperature maps on the object surface grid is proposed; this method maps a correspondence between 3D space coordinates and image coordinates and takes into account the directional emissivity by estimating the viewing angle. The advantages given by the use of the proposed method are shown with the application to a hypersonic wind tunnel test.

2 IR theory

Heat transfer by radiation is an energy transport mechanism that occurs in the form of electromagnetic waves. Via this heat transfer mode, energy can also travel in vacuum and may be partially absorbed and reflected by a body, or even pass through it. By denoting with α the radiation fraction being absorbed by the body, with ρ the fraction being reflected by it and with τ the fraction being transmitted (i.e., the fraction that passes through the object), the energy conservation law requires that

$$\alpha + \rho + \tau = 1 \tag{1}$$

where α, ρ and τ are, respectively, called absorptivity, reflectivity and transmissivity coefficients of the body under consideration. These coefficients may depend on both radiation wavelength and propagation direction.

According to the well-known Planck's law, the spectral radiance $I(\lambda)$ emitted by a body at temperature T and at wavelength λ is expressed as follows:

$$I(\lambda) = \varepsilon(\lambda) \frac{C_1}{\lambda^5 (e^{C_2/\lambda T} - 1)} \tag{2}$$

with $\varepsilon(\lambda)$ spectral emissivity and C_1, C_2 the first and the second universal radiation constants, respectively, equal to 3.7418×10^{-16} Wm^2 and 1.4388×10^{-2} mK.

Kirchhoff's law states that at thermal equilibrium the spectral emissivity coefficient is equal to the spectral absorptivity coefficient $\alpha(\lambda)$, which is the absorbed fraction of the radiation of wavelength λ. Therefore, for non-transparent bodies, such as those generally used in infrared thermography, Eq. (1) becomes:

$$\varepsilon(\lambda) + \rho(\lambda) = 1 \tag{3}$$

Real objects almost never emit in an isotropic way, the emissivity coefficient ε being dependent also on the angle θ (directional emissivity) between the direction of emission and the normal to the emitting surface (viewing angle). The

directional emissivity behavior of dielectric materials is quite different from metallic ones.

As shown in Fig. 1, at angles θ smaller than about 60°, dielectric materials have an almost constant and relatively high emissivity, while they emit poorly at large angles. On the contrary, electric conductors (such as metals) have usually a low emissivity, with a relative minimum in the normal direction. Since infrared measurements are often performed with dielectric materials at low θ values and because of the limited wavelength band captured by camera detectors, the emissivity of viewed surfaces is often assumed to be a constant. When it is necessary to work at high θ's, a careful calibration for ε as a function of θ must be performed and viewing angles have to be accurately known. A radiometer typically measures the spectral radiance emitted and the energy reflected by an object (in a given integration time and in a given wavelength that is typical of the sensor):

$$I^R = \tau \, \varepsilon(\theta) I^B_{obj} + \tau [1 - \varepsilon(\theta)] I^B_{amb} + (1 - \tau) I^B_{atm} \tag{4}$$

where τ is the transmissivity of the atmosphere between surface and camera, I^B_{amb} is the black body radiation intensity corresponding to the (actual) temperature T_{amb} of the environment surrounding the object called reflected ambient, or background, temperature (it is assumed that the ambient is a black body at a constant temperature and that the sensor surface is gray in the interested wavelength band, assumptions that can be mostly done in wind tunnel experiments), I^B_{atm} is the radiation intensity corresponding to a black body at the temperature of atmosphere T_{atm}, I^B_{obj} is the radiation intensity corresponding to a black body at the object temperature T_{obj}.
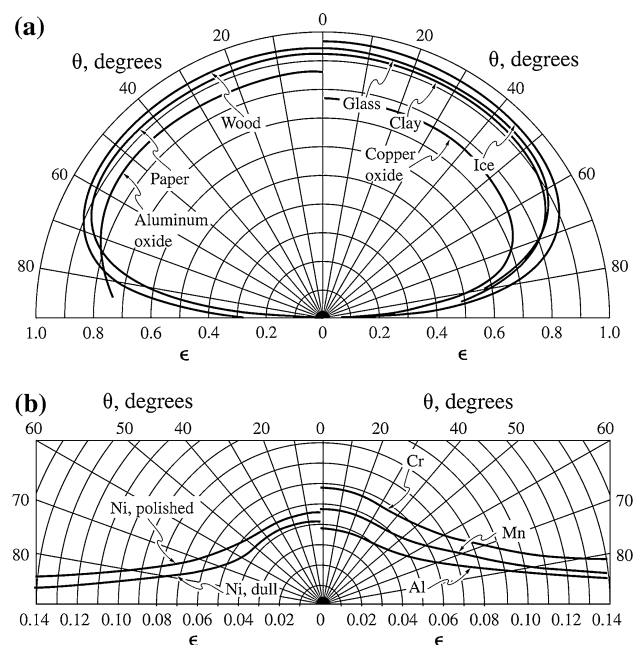

Fig. 1 Directional emissivity **a** for several non-metals; **b** for several metals. (From Schmidt and Eckert 1935)

For the sake of clarity in the Eq. (4) the dependence from λ is not indicated because usually the radiometer working wavelength (or band) is fixed. In Eq. (4), the term $\tau \varepsilon(\theta)\, I^{B}_{obj}$ is the emission from the surface captured by the radiometer, $\tau[1 - \varepsilon(\theta)]\, I^{B}_{amb}$ is the reflected emission from ambient sources, $[1 - \varepsilon(\theta)]$ being the surface reflectivity (T_{amb} is assumed to be constant for all emitting surfaces of the half sphere seen from the object surface); $(1 - \tau)\, I^{B}_{atm}$ is the emission from the atmosphere, $(1 - \tau)$ being the atmosphere emissivity. Typically the transmissivity of the atmosphere is assumed equal to unity simplifying Eq. (4).

From Eqs. (2) and (4) it is possible to obtain the semi-empirical adaptation of Planck's law with the constants R, B, F as reported by Ochs et al. (2009) and Carlomagno and Cardone (2010); the detected signal U_D is therefore:

$$U_{D} = \varepsilon(\theta)\frac{R}{e^{B/T_{obj}} - F} + [1 - \varepsilon(\theta)]\frac{R}{e^{B/T_{amb}} - F} \qquad (5)$$

where R is a function of IR camera integration time and wavelength, B is a function of IR camera wavelength and F is positive and its value is about 1.

3 Temperature maps reconstruction on 3D surfaces from IR images

In this paragraph the steps involved in the proposed approach to rebuild temperature maps onto a 3D surface grid from 2D IR images are described:

1. The choice of the camera model and of the calibration algorithm,
2. The calibration: the design of the target with IR control points (markers), the span of the investigated volume with the target, the determination of the real-world coordinates of these markers, the identification of the positions of the markers in the image plane and finally the determination of the parameters of the camera model (transformation between the real-world markers and their corresponding image locations),
3. The temperature maps reconstruction: the generation of a grid representative of the observed surface, the application of the camera model to the points of the grid to obtain the corresponding measured intensities, the evaluation of the viewing angle, the evaluation of the directional emissivity on the points of the grid and the computation of the surface temperature with the use of the calibration law on the grid points.

3.1 Camera calibration model

The camera model used in this work is based on a combination of linear and nonlinear techniques, in particular, on a perspective projection model with a correction for lens distortion (Heikkila 2000).

Consider a model of pure perspective projection, illustrated in Fig. 2. The centre of projection is the origin O of the image in the camera frame CF. The image plane Π is parallel to the xy plane and is placed at a distance f (focal length) from projection center O along the z axis; the z axis is also called *optical axis,* and the intersection with the plane Π is called the principal point o. The axes u and v of the 2D image frame IF are parallel to the axes x and y, respectively. The coordinates of o in IF are $[u_0, v_0]^T$. Let P be any point in the positive portion of z, and p its projection on the image plane. The coordinates of P in the world frame WF are $[X, Y, Z]^T$ while in the camera frame CF are $[x, y, z]^T$. The coordinates of p in IF are $[u, v]^T$ and can be given by the transformation:

$$\begin{bmatrix} u \\ v \\ 1 \end{bmatrix} \propto \underline{\underline{PM}} \begin{bmatrix} X \\ Y \\ Z \\ 1 \end{bmatrix} \qquad (6)$$

where $\underline{\underline{PM}}$ is the perspective transformation matrix with:

$$\underline{\underline{P}} = \begin{bmatrix} \xi f & 0 & u_0 & 0 \\ 0 & f & v_0 & 0 \\ 0 & 0 & 1 & 0 \end{bmatrix} \qquad (7)$$

where ξ is pixel aspect ratio and $\underline{\underline{M}}$ is a 4×4 matrix describing the transformation from WF to CF. The matrix $\underline{\underline{M}}$ is composed of a pure rotation and a translation as reported in Eq. (8).

$$\underline{\underline{M}} = \begin{bmatrix} \underline{\underline{R}} & \underline{t} \\ 0 & 1 \end{bmatrix} \qquad (8)$$
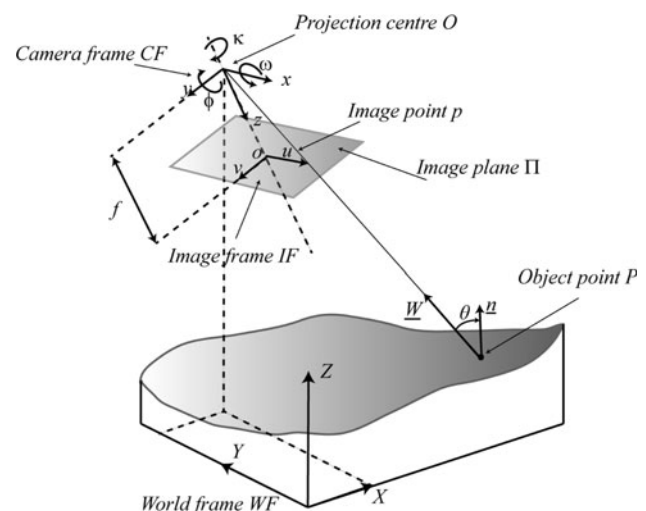

Fig. 2 Perspective projection model

where t describes the translation between the two frames, and $\underline{R}$ is a 3 × 3 orthonormal rotation matrix that can be defined by the three Euler angles ω, φ and κ. The parameters $\underline{t}$, ω, φ and κ are called extrinsic parameters or parameters of external projection, and the parameters ξ, f, u_0 and v_0 are the intrinsic parameters of the camera or internal projection parameters of the pinhole camera model. It is usually more convenient to express the coordinates of the image in pixels, so the coordinates obtained by Eq. (6) are multiplied by the factors D_u and D_v that specify the relationship between pixels and the physical units of the object, for example millimetres.

The perspective projection, typically, is not sufficient to exactly model real cameras. Ideally, light rays coming from the outside should move linearly in the optical centre of the lens, but in practice, the lens systems introduce nonlinear distortions in optical paths and in the resulting images. The perspective projection camera model gives the ideal image coordinates $[u, v]^{\mathrm{T}}$ of the projected point p. In order to distinguish these ideal coordinates from the equivalent distorted coordinates, henceforth the ideal coordinates are denoted with $[u_i, v_i]^{\mathrm{T}}$ and the distorted coordinates are denoted with $[u_{\mathrm{d}}, v_{\mathrm{d}}]^{\mathrm{T}}$.

The distorted coordinates are obtained by using a distortion model that decomposes the distortion in its radial and tangential parts (for a more detailed description see the work from Heikkila 2000). Only two radial distortion coefficients k_1 and k_2, and only two tangential distortion coefficients p_1 and p_2, are used, thus the distorted coordinates are as follows:

$$\begin{bmatrix} u_{\mathrm{d}} \\ v_{\mathrm{d}} \end{bmatrix} \cong \begin{bmatrix} u_i \\ v_i \end{bmatrix} - \underline{\Phi_D} \tag{9}$$

where

$$\underline{\Phi_D} = \frac{\begin{bmatrix} \overline{u_i}(k_1 r_i^2 + k_2 r_i^4) + 2p_1 \overline{u_i v_i} + p_2(r_i^2 + 2\overline{u_i^2}) \\ \overline{v_i}(k_1 r_i^2 + k_2 r_i^4) + p_1(r_i^2 + 2\overline{v_i^2}) + 2p_2 \overline{u_i v_i} \end{bmatrix}}{4k_1 r_i^2 + 6k_2 r_i^4 + 8p_1 \overline{v_i} + 8p_2 \overline{u_i} + 1},$$

$$r_i = \sqrt{\overline{u_i^2} + \overline{v_i^2}}, \overline{u_i} = u_i - u_0 \text{ and } \overline{v_i} = v_i - v_0.$$

3.2 The calibration target and the calibration procedure

The use of the proposed camera model to establish a correspondence between space coordinates and discrete image coordinates implies the need of a calibration process to estimate the parameters to perform this transformation. This purpose is generally accomplished with the help of a calibration target. This is typically a plane surface on which an array of equidistant points in two orthogonal directions is placed; once an origin has been set on this surface and the distance between the points is known, the physical coordinates of each point of the array is known; once an image has been recorded by the camera undergoing calibration, the coordinates of the points will be known also in the image frame. While the vision community generally makes use of checkerboard targets for camera calibration, the use of planar grids containing lines, dots or crosses is rather common in planar velocimetry calibration and for experimental fluid mechanics applications (Willert 2006). In either case, feature extraction algorithms recover the marker positions from the images and assign proper world (physical) coordinates to them. For the calibration tests described herein, grids of regularly spaced dots were used. Due to the symmetry of circular dots a detection scheme is easy to implement as well as more robust in off-axis or rotated viewing arrangements when compared to a grid of crosses or to a line grid. Experience has shown that, for the markers detection algorithms to work properly, the markers need to have a diameter of at least four/five pixels on the IR image.

The relative position between the calibration target and the observed object (model) has to be known. The target has to be moved along the whole volume in which the model will be situated, in order to acquire images in different known positions for the calibration and to map the observed volume. The positions of the control points are found within the images as the barycentre of the dots, evaluated using a threshold of the measured signal and, consequently, are known.

Once the space position and the image position of the control points are known, it is possible to apply the camera calibration algorithm. As proposed by Heikkila a linear algorithm (Abdel-Aziz and Karara 1971) is used to produce a first estimation. All the calibration constants are then found with a minimization of the root mean square difference between the known image coordinates of the control points and their image coordinates computed in accordance with the camera model. The minimization process is performed with the Levemberg-Marquardt method (Marquardt 1963) using as first trial value the first estimation computed with the linear algorithm. The success of the minimization process is reliant on an appropriate first trial value so the use of the parameters obtained with the linear algorithm is very useful.

The convergence of the minimization process is achieved when more than the theoretical minimum of 14 control points necessary are used and they are uniformly distributed across the investigated volume. This requirement can be obtained by acquiring several images of a plane calibration target (with at least 14 control points) spanning its normal direction in the investigated volume.

It must be noticed that the design of a target should guarantee that the markers are well visible from the IR camera both in terms of dimensions and in terms of their

features. For the applications in IR thermography described in this work, the contrast between the markers and the plane on which they are placed can be reached either using different emissivity or devising some method to keep the makers at a different temperature from the plane. Given the dependence of the target design on the particular experiment, detailed descriptions of the design procedures is postponed to the application section.

3.3 3D Surface temperature reconstruction

The first step of temperature reconstruction is the generation of the mesh on the surface of the object. The availability of an accurate surface grid is an important requirement, which may be achieved either by in-house or by commercially available software, depending on the complexity of the shape of the observed object. The mesh spacing has to be chosen to be just slightly higher than the spatial resolution of the IR camera, to avoid both loss of information and useless extra points (adding no further information but causing heavier computational load). The computed camera model constants are used to establish a correspondence between the points of the mesh and the pixels of the IR image. In that way it is possible to project the mesh points on the IR images and to evaluate the signal measured by the IR camera with an interpolation.

On the mesh points it is possible to evaluate the viewing angle, as done by Giordano and Astarita (2009). If the first-order Taylor series expansion of the calibration function is considered, a displacement $\underline{ds}$ in the image plane Π can be expressed as the product of the derivate of the calibration function by an infinitesimal space displacement $\underline{dS}$:

$$\underline{ds} = \begin{bmatrix} u_X & u_Y & u_Z \\ v_X & v_Y & v_Z \end{bmatrix} \cdot \underline{dS} = \begin{bmatrix} u_X & u_Y & u_Z \\ v_X & v_Y & v_Z \end{bmatrix} \cdot \begin{bmatrix} dX \\ dY \\ dZ \end{bmatrix} \tag{10}$$

In order to determine the local viewing angle an infinitesimal displacement vector $\underline{dS}$ along the viewing ray of the camera can be imagined. Obviously the correspondent displacement $\underline{dS}$ in the image plane is zero.

The solution of this equation gives the viewing ray direction $\underline{W}$ as represented in Fig. 2:

$$\left.\frac{dX}{dZ}\right|_{\underline{ds}=0} = \frac{v_Z u_Y - v_Y u_Z}{v_Y u_X - v_X u_Y} \quad \left.\frac{dY}{dZ}\right|_{\underline{ds}=0} = \frac{v_Z u_X - v_X u_Z}{v_X u_Y - v_Y u_X} \tag{11}$$

Infact by choosing $dZ = 1$ it is possible to determine the normalized vector of the viewing ray direction.

$$\underline{W} = \begin{bmatrix} \left.\frac{dX}{dZ}\right|_{\underline{ds}=\underline{0}} & \left.\frac{dY}{dZ}\right|_{\underline{ds}=\underline{0}} & 1 \end{bmatrix} \tag{12}$$

With a scalar product of the viewing ray direction by the known normal unit vector $\underline{n}$ on the object surface, the viewing angle θ on the object surface is easily evaluated.

$$\theta = \cos^{-1} \left| \frac{\underline{W} \cdot \underline{n}}{|\underline{W}|} \right| \tag{13}$$

As said before, the surface emissivity depends on viewing angle. Once the viewing angle is estimated, it is possible to correct the emissivity value with a law that relates emissivity to the viewing angle. A model reported by Siegel and Howell (1992) and Ianiro and Cardone (2010) relates emissivity to the refraction index and to the extinction coefficient (the imaginary part of the complex index of refraction).

The value of the temperature for every grid point is finally evaluated according to Eq. (14)

$$T = \frac{B}{\ln\left\{\dfrac{\varepsilon(\theta) \cdot R}{\left[U_D - (1-\varepsilon(\theta))\dfrac{R}{e^{B/T_{amb}}-F}\right]} + F\right\}} \tag{14}$$

4 Application: temperature maps reconstruction on a double cone in hypersonic wind tunnel testing

The experimental campaign illustrated in this paragraph is aimed at an analysis of the shock wave boundary layer interaction; this is a key phenomenon to be studied in the design of hypersonic vehicles both because of the high loads on the interested surfaces and because it typically occurs over the control surfaces of hypersonic vehicles, where flow separation and recirculation can have significant effects on their efficiency. A sharp, double-cone geometry has been selected for the test case; the hypersonic flow over a double-cone geometry produces many of the complex phenomena that take place in flows past hypersonic vehicles, such as shock interactions, triple points, and recirculation zones. Double-cone geometries have therefore been subject of extensive studies both experimental and numerical (Wright et al. 2000, Druguet et al. 2005). The double-cone geometry, despite of its simplicity, is clearly non-planar and represents an idoneous test case for the proposed methodology because the measurements are affected by viewing angle variations.

A schematic description of the hypersonic flow past a double cone, following Druguet et al. (2005), is given in Fig. 3.

The attached leading-edge shock wave interacts with a detached bow shock wave formed from the second cone, and this interaction produces a transmitted shock wave that impinges on the second cone surface, where very high surface pressures and heat transfer rates are consequently generated. Because of the high pressures at the impingement location, the flow separates near the cone–cone juncture and a recirculation zone develops, which in turn alters the shock interaction. The size of the separation zone
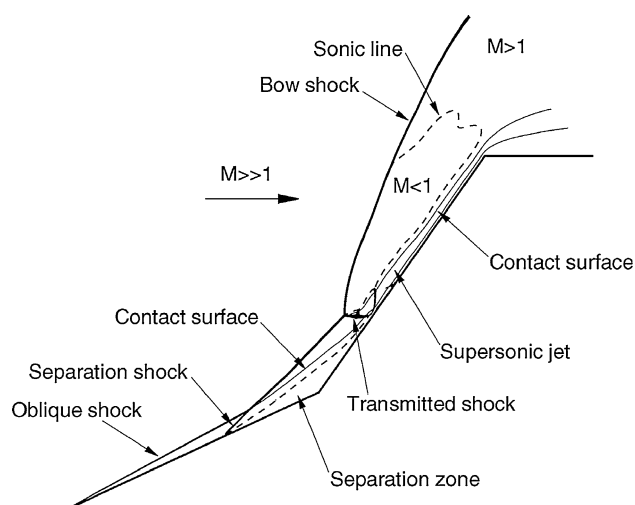
Fig. 3 Schematic of the hypersonic flow past a double-cone geometry (from Druguet et al. 2005)

Table 1 Characteristics of the FLIR SC3000 IR camera

Detector type	GaAs QWIP, 320 × 240 pixels
Spectral range	8–9 μm
Field of view	20° × 15°
IFOV	1.1 mrad
Frequency of acquisition	60 Hz non interlaced up to 750/900 Hz with image binning
Temperature range	−20 to +500°C. up to 2,000°C with filters
NETD	20 mK at ambient temperature
Accuracy	±1% or ± 1°C (for measurement ranges up to +150°C)
	±2% or ± 2°C (for measurement ranges above +150°C)
Intensity resolution	14 bit

is very sensitive to the shock angles and to the strength of the shock interaction. Downstream of the shock impingement location, a supersonic jet develops near the second cone surface. From an aerothermal point of view the points of greatest interest are the separation zone around the connection between the two cones and the reattachment on the second zone; these should be clearly visible on model thermal maps, because the recirculation involves reduced heat transfer, and consequent reduced surface heating, while a peak in heating is obviously expected at the reattachment point.

The test has been performed in the High Enthalpy Archeated Tunnel (HEAT), Alta's small hypersonic wind tunnel (Fig. 4), operative since 1996 in the low–medium unit Reynolds number range, 10^4–10^6 m^{-1} (Biagioni et al.
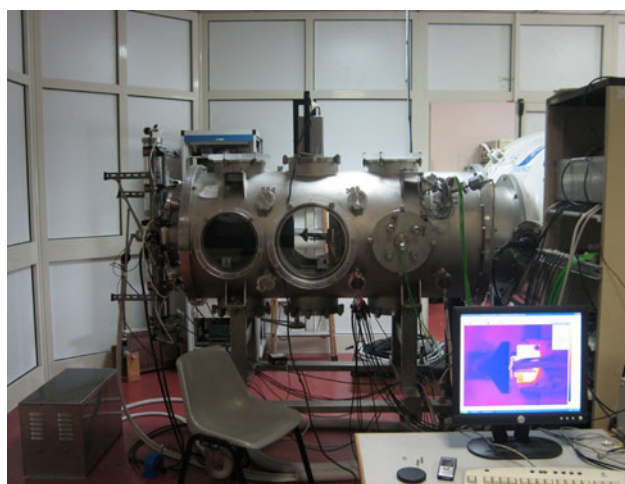

Fig. 4 The HEAT facility in ALTA (Pisa). It is possible to see the thermograph mounted on the *top* of the wind tunnel, the model inside the test chamber and the IR image of the model

1999). The flow total pressure in air can vary typically between 1 and 9 bar, with total enthalpy up to 6 MJ/kg. Two contoured nozzles can be used in air to produce flows at Mach number equal to 6 and 9. The typical test duration is between 50 and 300 ms, limited only by the vacuum chamber back pressure.

A dedicated flange with a Germanium window is installed on the tunnel wall above the model for use with IR thermography. The window, inclined with respect to the axis of observation to avoid any reflection on the camera, is coated with anti-reflection materials for the long wave range (8–14 μm). According to the analysis of the characteristics of plasmas emission in high enthalpy wind tunnels and of the associated choice of the appropriate IR band, reported by Cardone (2007), a FLIR SC3000 thermograph has been used for temperature measurements. A list of the main characteristics of the SC3000 can be found in Table 1. For this work, an accurate calibration (simulating the entire optical path between the camera and the observed object) was performed with a blackbody at known temperature. In particular, the values of the IR signal detected from the camera were fitted with the law in Eq. (5) in order to evaluate the constants R, B and F. The temperature variation of the window was considered as negligible due to the short duration of the present test, so the calibration was done with the window at ambient temperature; in case of tests with longer time duration it can be necessary to take into account the window heating.

The model, expressly designed for the test, has an internal aluminium structure covered by a MACOR® shell of 1.5 mm of thickness. The sharp leading edge was made of stainless steel in order to avoid erosion during the experiments and to keep the conic shock wave attached.

The geometry, inspired by the geometry used by Druguet et al. (2005) shown in Fig. 5, is therefore characterized by semi-aperture angles of the cone of 25 and 55 degrees. The linear dimensions have instead been scaled in

Fig. 5 The double-cone model picture

Fig. 6 MACOR® directional emissivity at 8–9 μm

order to place the whole model within the core flow with uniform Mach number. The base diameter of the first cone and of the second cone has been set, respectively, to 23 and 70 mm. The base diameter of the stainless steel tip, on which IR measurements are not possible, has been set to 6.5 mm

With regard to the emissivity ε of MACOR® it is highly dependent on surface finish and may also vary considerably. Therefore, the data in literature are not entirely reliable and an emissivity characterization was necessary. This characterization is also needed to measure the directional emissivity, which can play a crucial role in the present experiment where there are high observation angles, especially in the case of the cone with a semi-aperture angle of 55 degrees.

A full characterization for the directional emissivity was conducted in DIAS laboratory comparing the energy emitted by a blackbody and a sample of MACOR® (with the same surface finish of the MACOR® used for the model) in the IR band characteristic of the camera and are fitted according to the directional emissivity law reported by Ianiro and Cardone 2010. The results are shown in Fig. 6.

The design of the target needed for the geometrical reconstruction, as said before, is strictly linked with the test in which it has to be used. In particular, it must take into account the dimensions of the model, the resolution of the IR camera and the distance between the camera and the model. The parameters of interest are as follows:

- Pixel image size: 320×240 pixels,
- Aperture of the lens on the SC3000: $25° \times 20°$
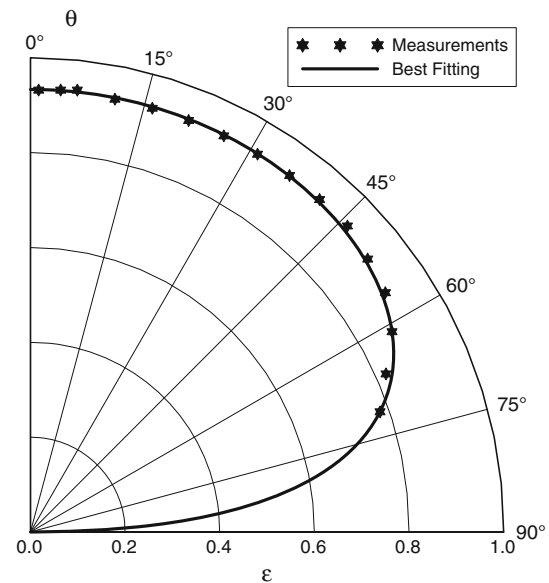- Distance of the SC3000 from the model: ~ 500 mm

These data allow calculating the spatial resolution on the surface of the model, which is about 0.5 mm and that a maximum total area of 16×12 cm will be seen: Starting from this information, the dimensions of the target can be set: a 12×12 cm flat slab with thermal markers of 2.2 mm diameter has been chosen. As said previously, in order to be visible the thermal markers need to have as large a different emissivity as possible from that of the background. The choice to have high emissivity markers on a low emissivity slab is made, on the basis of considerations on the ease of manufacturing.

A surface of polished aluminium has been chosen as background, and the markers have been realized by drilling holes of 10 mm of depth in it. Holes whose depth is more than 4 times the diameter have very high emissivity (in this case higher than 0.95), thanks to the fact that multiple reflections inside the hole let emerge from it only a tiny part of the incident radiation (Wolfe and Zissis 1989).

The target can be heated quickly and very easily, thanks to its small dimensions, and it is characterized by high-temperature uniformity, thanks to the high conductivity of the aluminium. When the target is heated, the thermal markers are clearly seen as hot spots on a cold surface. A picture of the target is shown in Fig. 7a, and its thermal map is shown in Fig. 7b. It has to be remarked that when sting and model oscillation are not negligible, it can be helpful to use markers on the real model in order to correct the target calibration.

The target, the model support system and the model (double cone) have been designed in such a way that the vertex of the cone coincides with the centre of one of the thermal markers when the target lies on one of its

Fig. 7 a Picture of the target; **b** IR image of the target
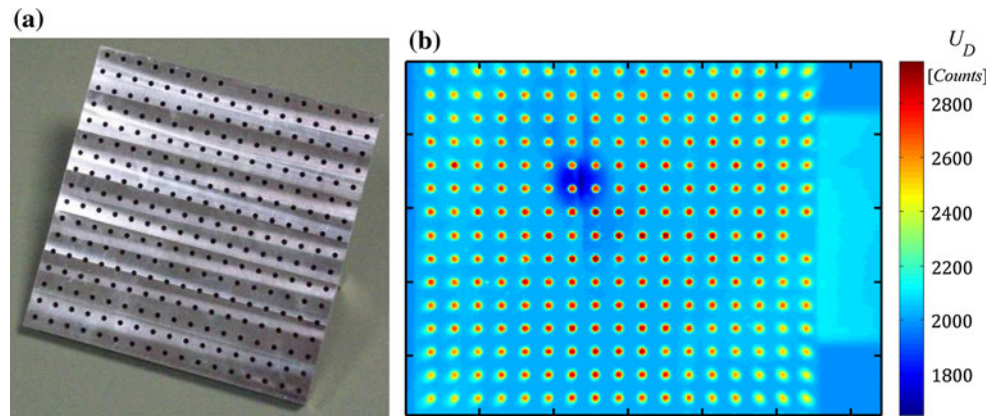
calibration planes. It is noted that the resection process has a sub-pixel precision; in particular, for the present test the root mean square error is 0.2067 pixels. In the same conditions, neglecting the lens distortion effect, the root mean square error is 0.5324 pixels. This error can dramatically increase if lower quality lenses or more complex optical paths are used. The experiments were carried out with synthetic air flow (80% N2, 20% O2) with a total pressure of 3 *bar,* a total enthalpy of 4.5 MJ/kg and a Mach number equal to 9.3. A time sequence of IR images was acquired at full frame at a frequency of 60 Hz; in Fig. 8 an IR image of double-cone model is shown. During the test campaign some IR sequences were also acquired at a reduced frame size of 320 × 48 in order to increase the frame rate up to 300 Hz for the purpose of heat transfer calculations. For more information about heat transfer values measured in this experimental campaign, please refer to dello Ioio (2008).

The double-cone geometry is quite simple to discretize, and a mesh has been generated with an in-house code. The mesh spacing has been chosen to be just slightly higher

than the spatial resolution of the thermograph. As shown in Fig. 6, the emissivity of MACOR® decreases dramatically for viewing angle θ higher than 70°; as a consequence, the mesh has been generated only on a limited sector of the double cone (±40° angle from the vertical direction Z), and the other points of the surface cone seen by the thermograph have not been used for temperature measurements. Figure 9 shows the mesh built on the cone. Figure 10 shows an IR image of the model with the projection of the points of the mesh superimposed.

As explained before the viewing angle was also calculated. Once the viewing angles are known by Eq. (13), the emissivity of the model on each point of the mesh is calculated according to the law reported by Ianiro and Cardone 2010. A map of emissivity is shown in Fig. 11.

Finally, temperatures on the grid are calculated with Eq. (14) using the values of U_D interpolated on the mesh nodes. Figure 12 shows the 3D surface temperature map just before the end of the blowdown shot, when maximum heating is reached. Separation and reattachment can be
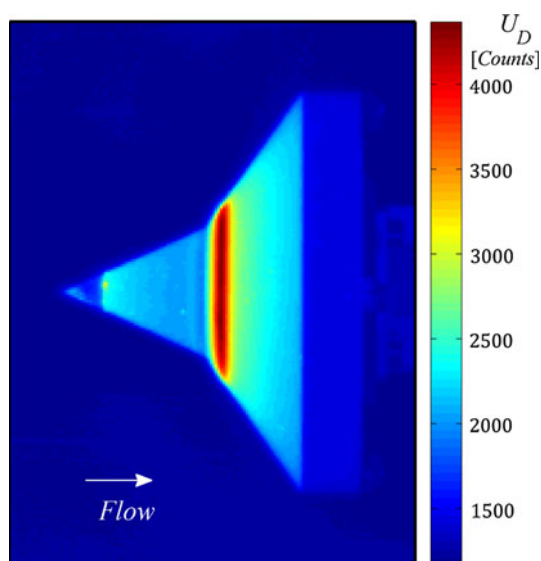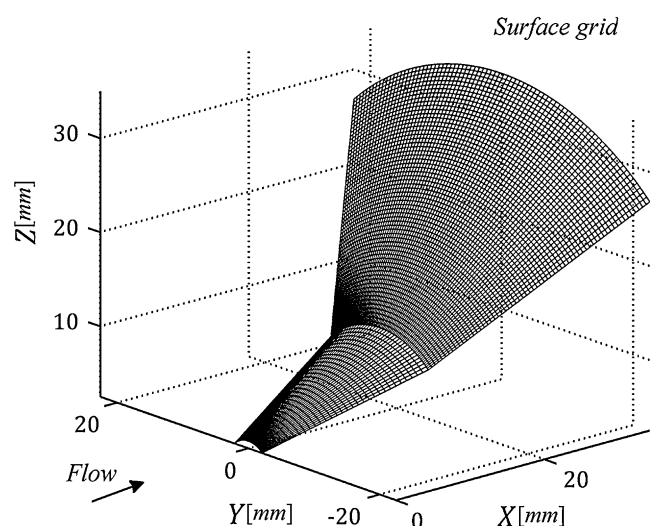

Fig. 8 A typical IR image

Fig. 9 The double-cone surface grid. Only a sector of 30° around the Z axis is considered and the stainless steel tip is not meshed
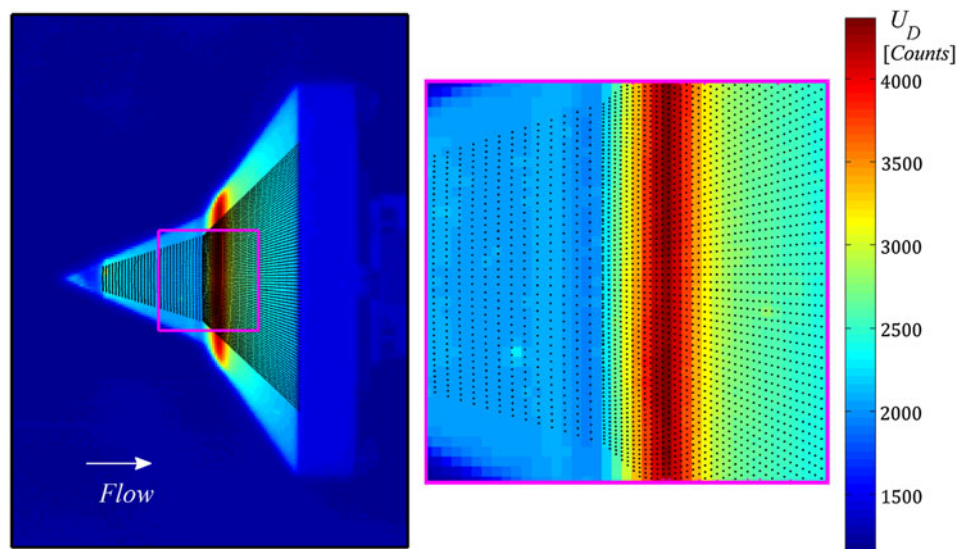
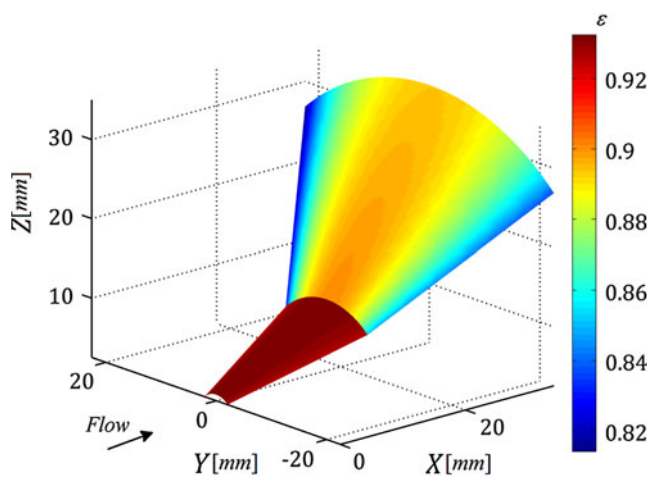**Fig. 10** The mesh of Fig. 9 projected on the IR image in Fig. 8

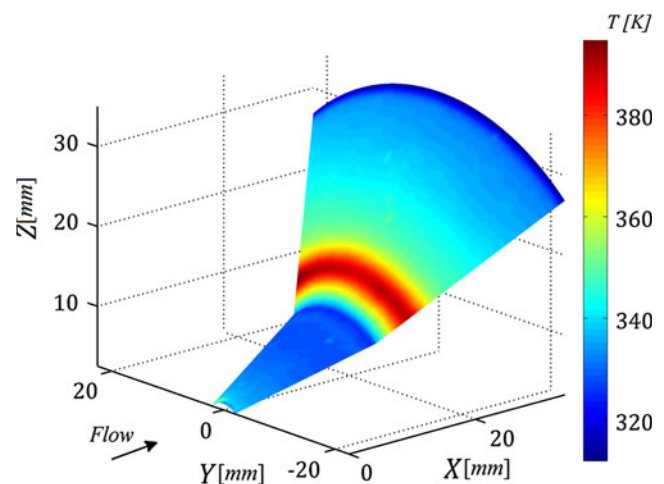**Fig. 11** Measured directional emissivity map

Fig. 12 3D surface temperature map just before the end of the blowdown shot, time = 0.1 s

seen well from the 3D temperature map. The separation zone at the end of the first cone is visible, being colder, and the reattachment zone is visible too, being at a significantly higher temperature.

5 Conclusions

In this work an optical geometric calibration is successfully applied to IR thermography in order to rebuild temperature maps of 3D surface models in wind tunnel experiments.

The adopted camera model is a perspective projection model with lens distortion correction, and the optical calibration is done by means of a novel IR target plate. The

general rules for the design of the target, the evaluation of the camera model constants and the object surface discretization are analyzed and discussed. The proposed methodology allows estimating the camera viewing angle thus increases the accuracy of temperature measurements taking into account the directional emissivity.

An experimental application of the proposed method in a hypersonic wind tunnel is presented and discussed in detail. A sharp, double-cone geometry has been selected as test case because it produces many complex phenomena, such as shock interactions, triple points and recirculation zones. The double-cone geometry, despite of its simplicity, is clearly non-planar and represents an idoneous test case for the proposed methodology because the measurements

are affected by viewing angle variations. The root mean square error due to mapping is shown to be about 0.2 pixels in the tested conditions, thus it is evident as the results of this work can have significant impact on the understanding of the physics associated with the surface topology of complex flows on highly three-dimensional models.

References

Abdel-Aziz YI, Karara HM (1971) Direct linear transformation from comparator coordinates into object space coordinates in close-range photogrammetry. Proceedings of the Symposium on Close-Range Photogrammetry. American Society of Photogrammetry, Falls Church, pp 1–18

Biagioni L, Scortecci F, Paganucci F (1999) Development of pulsed arc heater for small hypersonic high-enthalpy wind tunnel. J Spacecr Rocket 36(5):704–710

Brown DC (1971) Close-range camera calibration. Photogramm Eng 37(8):855–866

Büyüksalih G (2003) Geometric calibration models of infrared cameras and scanners for photogrammetric and remote sensing applications. Opt Eng 42(7):1923–1934

Cardone G (2007) IR heat transfer measurements in hypersonic plasma flows. QIRT J 4(2):233–251

Carlomagno GM, Cardone G (2010) Infrared thermography for convective heat transfer measurements. Exp Fluids 49(6): 1187–1218

de Luca L, Cardone G, Carlomagno GM, Aymer de la Chevalerie D, Alziary de Roquefort T (1992) Flow visualization and heat transfer measurement in a hypersonic wind tunnel. Exp Heat Transfer 5(1):65–78

de Luca L, Cardone G, Aymer de la Chevalerie D et al (1995) Viscous interaction phenomena in hypersonic wedge flow. AIAA J 33(12):2293–2298

dello Ioio G (2008) An improved data reduction technique for heat transfer measurements in hypersonic flows. PhD Thesis, Università degli Studi di Napoli "Federico II"

DeWitt DP, Nutter GD (1989) Theory and practice of radiation thermometry. Wiley, New York

Druguet MC, Candler GV, Nompelis I (2005) Effect of numerics on Navier-Stokes computations of hypersonic double-cone flows. AIAA J 43(3):616–623

Faugeras O, Toscani G (1986) The calibration problem for stereo. Proceedings of the 1986 conference on computer vision and pattern recognition (CVPR '86): 15–20

Giordano R, Astarita T (2009) Spatial resolution of the stereo PIV technique. Exp Fluids 46(4):643–658

Heikkila J (2000) Geometric camera calibration using circular control points. IEEE Trans Pattern Anal Mach Intell 22(10):1066–1077

Heikkilä J, Silven O (1997) A four-step camera calibration procedure with implicit image correction. Proceedings of the 1997 conference on computer vision and pattern recognition (CVPR '97): 1106–1112

Ianiro A, Cardone G (2010) Measurement of surface temperature and emissivity with stereo dual-wavelength IR thermography. J Mod Opt 57(18):1708–1715

Le Sant Y (2005) An image registration method for infrared measurements. QIRT J 2(2):207–222

Le Sant Y, Marchand M, Millan P, Fontaine J (2002) An overview of infrared thermography techniques used in large wind tunnels. Aerosp Sci Technol 6(5):355–366

Marquardt D (1963) An algorithm for least-squares estimation of nonlinear parameters. SIAM J Appl Math 11(2):431–441

Ochs M, Horbach T, Schulz A, Koch R, Bauer HJ (2009) A novel calibration method for an infrared thermography system applied to heat transfer experiments. Meas Sci Technol 20:1–9

Schmidt E, Eckert E (1935) Über die Richtungsverteilung der Wärmestrahlung von Oberflächen. Forschung im Ingenieurwesen 6(4):175–183

Siegel R, Howell JR (1992) Thermal Radiation Heat Transfer, 3rd edn. Hemisphere, Washington

Tsai RY (1987) A versatile camera calibration technique for high-accuracy 3D machine vision metrology using off-the-shelf TV camera and lenses. IEEE J Robotics Autom 3(4):323–344

Weng J, Cohen P, Herniou M (1992) Camera calibration with distortion models and accuracy evaluation. IEEE Trans Pattern Anal Mach Intell 14(10):965–980

Willert C (2006) Assessment of camera models for use in planar velocimetry calibration. Exp Fluids 41(1):135–143

Wolfe WL, Zissis GJ (1989) The infrared handbook. Office of Naval Research, Department of the Navy, Arlington

Wright MJ, Sinha K, Olejniczak J, Magruder TD, Smits AJ (2000) Numerical and experimental investigation of double-cone shock interactions. AIAA J 38(12):2268–2276